ICCFD13-2026-327

BYCSprayFoam: An Efficient Euler–Lagrange Solver for Gas–liquid Two-Phase Rotating Detonation Engines

Yiting Dang*, Yangfan Zhou*, Ao Xiong*, Shengyang Li*,
John Z. Ma*, and Jianping Wang*
Corresponding author: wangjp@pku.edu.cn
* Center for Combustion and Propulsion, SKLTCS, School of Mechanics and Engineering Sciences, Peking University, China.

Abstract: BYCSprayFoam is an OpenFOAM-based Euler–Lagrange solver developed for gas–liquid two-phase rotating detonation engine (RDE) simulations. Built on OpenFOAM-v1812, it extends the gas-phase solver BYCFoam by incorporating two-way coupled Lagrangian spray parcels with interphase mass, momentum, energy, and species exchange. Thermodynamic, transport, and finite-rate chemistry properties are evaluated through Cantera, enabling species-dependent NASA-polynomial thermochemistry and mixture-averaged transport for multispecies reacting flows. The solver supports multiple shock-capturing flux schemes, operator-splitting-based chemistry integration, adaptive mesh refinement, and mesh/chemistry load balancing for efficient detonation simulations with localized stiffness and strong flow discontinuities. The solver is first verified using single-droplet evaporation, heat-transfer, and velocity-relaxation cases, showing improved heat- and mass-transfer predictions compared with OpenFOAM-native thermophysical treatments while retaining accurate momentum coupling. One- and two-dimensional n-decane detonation-tube simulations are then performed to validate detonation velocity, CJ pressure ratio, and cell size against experimental and theoretical references for both gas-phase and spray mixtures. The results show that BYCSprayFoam accurately captures key CJ characteristics and the enlarged effective induction-zone length in spray detonations. A two-dimensional wedge-induced standing-detonation case further demonstrates that adaptive mesh refinement and load balancing reduce computational cost by approximately a factor of four without altering the predicted flow structure. Finally, a three-dimensional non-premixed spray RDE simulation is conducted, in which a self-sustained rotating detonation wave is obtained. These results demonstrate that BYCSprayFoam provides an accurate and efficient computational framework for gas–liquid two-phase rotating-detonation simulations.

Keywords: Rotating Detonation, OpenFOAM, Cantera, Euler–Lagrange.

1. Introduction

Detonation-driven reacting flows are challenging because they combine strong shocks, thin reaction zones, and stiff finite-rate chemistry, which together impose stringent stability and accuracy constraints on the physical time step [1]. Rotating detonation engines (RDEs) are a representative pressure-gain combustion concept with the potential to outperform conventional constant-pressure combustors in thermal efficiency [2, 3], and recent efforts have moved from proof-of-concept toward engineering-oriented validation and benchmarking [4]. In parallel, liquid kerosene fuels have been increasingly investigated and demonstrated in rotating detonation configurations due to their portability and high volumetric energy density [5, 6]. These trends motivate efficient simulation tools for gas–liquid two-phase RDEs, where robust two-way spray coupling must coexist with shock-capturing numerics and stiff chemistry at scale [1, 7].

OpenFOAM provides a widely used open-source framework for compressible reacting-flow development. Recent detonation solvers have shown that appropriate chemistry coupling strategies, and

parallel load-balancing methods can substantially improve simulation efficiency, as demonstrated by detonationFoam [1] and our earlier BYCFoam [7]. For spray-driven detonation/RDE problems, an Euler–Lagrange formulation is often preferred for dilute dispersed phases, solving the carrier gas in an Eulerian finite-volume framework while tracking droplets as Lagrangian parcels with two-way interphase source terms [8]. This direction has been explored in OpenFOAM-based detonative solvers such as RYrhoCentralFoam [9] and CDSFoam [10], and it also exposes the main computational bottlenecks in rotating-detonation applications, including stiff chemistry and small time steps induced by locally refined cells. Operator splitting [11] offers a practical route to decouple transport from chemistry and enables scalable cell-local chemistry integration. Motivated by these considerations, we develop BYCSprayFoam, an efficient OpenFOAM-based Euler–Lagrange solver for gas–liquid two-phase rotating-detonation simulations, by extending BYCFoam.

2. Methodology

BYCSprayFoam is developed on OpenFOAM v1812 by extending our gas-phase rotating-detonation solver BYCFoam [7] to an Euler–Lagrange spray framework [8]. The Eulerian gas phase is governed by compressible multispecies conservation laws for mass, momentum, total energy, and species, augmented by interphase source terms that represent the cell-averaged mass, momentum, energy, and species exchanges contributed by the Lagrangian parcels. Thermodynamic closure is provided by the ideal-gas equation of state, and the energy equation is formulated in terms of sensible quantities to account consistently for gas-phase heat release and diffusive enthalpy transport. The governing equation for the Euler fields is written as

$$\begin{aligned}
&\frac{\partial \rho}{\partial t} + \boldsymbol{\nabla} \cdot (\rho \boldsymbol{u}) = S_{\mathrm{mass}} \\
&\frac{\partial (\rho \boldsymbol{u})}{\partial t} + \boldsymbol{\nabla} \cdot (\rho \boldsymbol{u}\boldsymbol{u}) + \boldsymbol{\nabla} p = \boldsymbol{\nabla} \cdot \boldsymbol{\tau} + \boldsymbol{S}_{\mathrm{mom}} \\
&\frac{\partial (\rho E)}{\partial t} + \boldsymbol{\nabla} \cdot [(\rho E + p)\boldsymbol{u}] = \boldsymbol{\nabla} \cdot (\boldsymbol{\tau} \cdot \boldsymbol{u}) - \boldsymbol{\nabla} \cdot \boldsymbol{q}_{\mathrm{s}} + S_{\mathrm{energy}} \\
&\frac{\partial (\rho Y_k)}{\partial t} + \boldsymbol{\nabla} \cdot (\rho Y_k \boldsymbol{u}) = \dot{\omega}_k - \boldsymbol{\nabla} \cdot \boldsymbol{j}_k + S_{\mathrm{species},k}
\end{aligned},$$

where t denotes time; ρ, $\boldsymbol{u}$, and p are the density, velocity, and pressure of the gas mixture; $\boldsymbol{\tau}$ is the viscous stress tensor (the mixture is treated as a Stokes fluid); E is the total energy per unit mass; $\boldsymbol{q}_{\mathrm{s}}$ is the heat flux; $\boldsymbol{j}_k$ is the diffusive mass flux of species k; Y_k is the mass fraction; and $\dot{\omega}_k$ is the net chemical production rate.

For the dispersed phase, particles are packed into parcels that are tracked in a Lagrangian manner:

$$\frac{\mathrm{d}m_{\mathrm{d}}}{\mathrm{d}t} = \dot{m}_{\mathrm{d}}, \qquad \frac{\mathrm{d}\boldsymbol{u}_{\mathrm{d}}}{\mathrm{d}t} = \frac{\boldsymbol{F}_{\mathrm{d}}}{m_{\mathrm{d}}}, \qquad c_{p,\mathrm{d}} \frac{\mathrm{d}T_{\mathrm{d}}}{\mathrm{d}t} = \frac{\dot{Q}_{\mathrm{c}} + \dot{Q}_{\mathrm{lat}}}{m_{\mathrm{d}}}.$$

In the equation, the particle mass m_{d} (assuming spherical particles) evolves according to a mass-change rate that is solely attributed to evaporation; the standard sub-models available in OpenFOAM can be employed for these closures.

For thermodynamic, transport, and chemistry evaluations, BYCSprayFoam is coupled with Cantera (v2.5.1) [12]. Thermodynamic properties are evaluated using JANAF/NASA-7 polynomials with species-dependent midpoint temperatures, avoiding the globally fixed midpoint commonly assumed by native OpenFOAM thermodynamics and improving fidelity for fuels with pronounced negative-temperature-coefficient behavior. Species transport coefficients are computed from kinetic-theory-based models and combined using Cantera mixture-averaged transport [12], providing a more general alternative to common OpenFOAM defaults such as Sutherland viscosity, the Eucken approximation, and unity-Schmidt-number assumptions [13, 14]. Chemical source terms are integrated through Cantera

with the SUNDIALS ODE suite, and operator splitting [11] is used so that chemistry is advanced independently in each cell. This structure facilitates parallel efficiency measures by redistributing chemistry workloads from heavily loaded to lightly loaded processes when detailed mechanisms are used.

BYCSprayFoam supports several shock-capturing convective fluxes, including the Kurganov [15], HLL [16], HLLC [17], and AUSM+M [18] schemes. Diffusive terms use a second-order central scheme. Time integration includes the standard Euler and backward schemes in OpenFOAM, as well as a dual time-stepping (DTS) method [19] that solves the implicit physical-time update through pseudo-time iterations with local time stepping and consistent Eulerian-Lagrangian coupling.

To reduce computational cost while preserving resolution in shock-reaction regions, BYCSprayFoam supports h-adaptive mesh refinement (AMR) [20], using octree refinement in 3D and quadtree refinement in 2D. Refinement and coarsening use parent-to-child injection and child-to-parent volume-weighted restriction, respectively, and multiple indicators based on field magnitudes and gradient norms can be combined. In parallel computations, load balancing can be applied periodically to mitigate imbalance introduced by mesh adaptation. For workflow flexibility, swak4Foam [21] is integrated to enable runtime post-processing through algebraic expressions without additional C++ coding, and it is compatible with the Eulerian fields, Lagrangian parcels, Cantera coupling, and AMR modules.

The overall framework of BYCSprayFoam is shown in Figure 1.

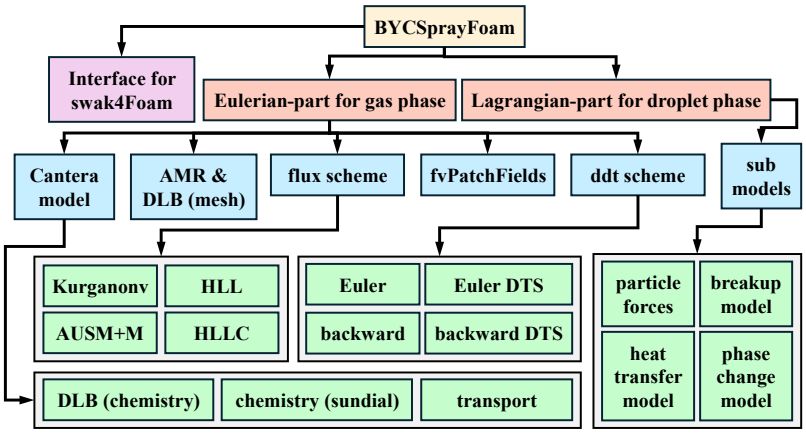

Figure 1: The main framework of BYCSprayFoam.

3. Results

This section validates the accuracy and acceleration performance of BYCSprayFoam. The validation first examines single-droplet Lagrangian submodels, then assesses the chemical-reaction model using one- and two-dimensional detonation-tube cases. The computational acceleration strategies are subsequently evaluated, and a three-dimensional spray RDE simulation is finally presented.

3.1. Validation of the droplet Lagrangian submodels

Single-droplet evaporation, heat-transfer, and velocity-relaxation problems were simulated for water droplets. The results are shown in Figures 2–4.

In the single-droplet evaporation case, a suspended water droplet with an initial diameter of 1.047 mm and an initial temperature of 282 K evaporates in air at 298 K and 1.01325 bar. This problem follows the classical d^2-law, in which the square of the droplet diameter decreases linearly with time until complete evaporation. As shown in Figure 2, the BYCSprayFoam prediction follows the d^2-law and is closer to the experimental result than previously reported numerical results. This verifies the accuracy of the liquidEvaporation model and its coupling with the Cantera thermodynamic module.

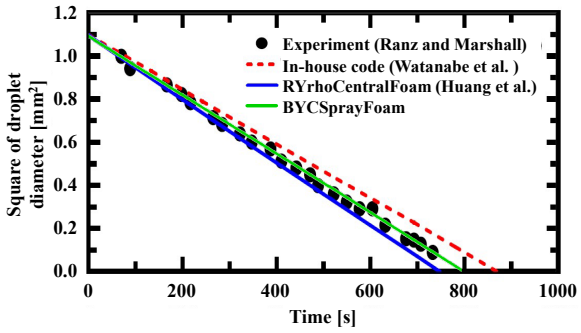

Figure 2: Single-droplet evaporation case. Data are from Ranz and Marshall [22], Watanabe et al. [23], and Huang et al. [9].

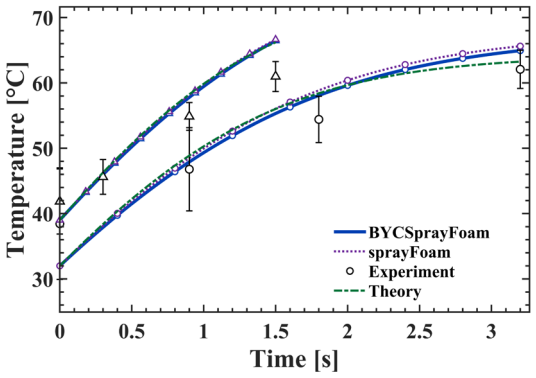

Figure 3: Single-droplet heat-transfer case. Experimental and theoretical data are from [24].

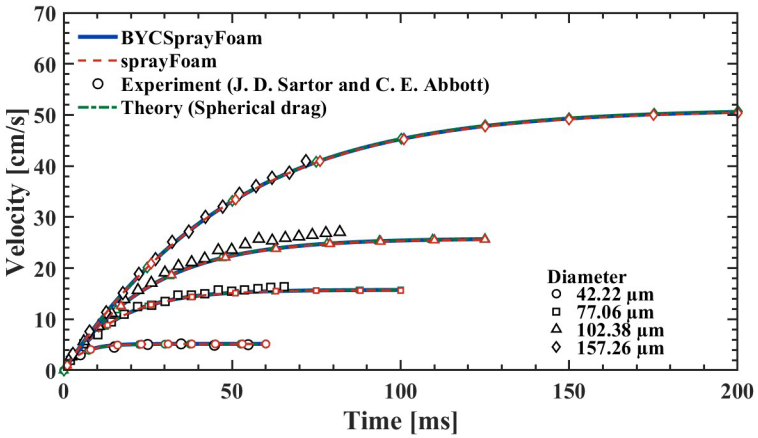

Figure 4: Single-droplet velocity-relaxation case. Experimental data are from [25].

In the single-droplet heat-transfer case, a water droplet with an initial diameter of 3.06 mm is placed in air at 1.01325 bar. Two conditions are simulated: in the first, the initial droplet and air temperatures are 305.15 K and 773.15 K, respectively; in the second, they are 312.15 K and 1073.15 K, respectively. Figure 3 shows that BYCSprayFoam agrees more closely with the experimental and theoretical predictions than the sprayFoam solver in OpenFOAM-v1812. The remaining discrepancy is mainly attributable to heat conduction from the droplet to the supporting rod in the experiment. The theoretical solution is obtained from the model proposed in [24]. This case further verifies the liquidEvaporation model and its coupling with Cantera-based gas properties.

In the single-droplet velocity-relaxation case, water droplets with diameters of 42.22, 77.06, 102.38, and 157.26 µm are initially at rest in air at 295.15 K and 1.01325 bar and are accelerated by gravity (g = 9.81 m/s). As shown in Figure 4, BYCSprayFoam and sprayFoam give nearly identical predictions, both of which agree well with the experimental and theoretical solutions. This validates the drag model in OpenFOAM-v1812 and its coupling with the Cantera-based gas-phase module.

These validation cases show that, compared with existing solvers based on OpenFOAM native thermophysical properties, BYCSprayFoam improves accuracy for interphase mass and heat transfer while retaining comparable accuracy for momentum exchange. The improvement mainly results from the use of Cantera to evaluate gas-phase thermodynamic properties, including specific internal energy, enthalpy, heat capacities, and entropy, as well as transport coefficients such as mass diffusivity, thermal diffusivity, and dynamic viscosity. Tables 1 and 2 compare the OpenFOAM and Cantera treatments. The dominant differences arise in the transport coefficients: BYCSprayFoam uses kinetic-theory-based,

mixture-averaged transport, thereby avoiding the potentially large errors introduced by the unity-Lewis-number assumption and by direct use of the Eucken approximation for diffusivity-related quantities.

Table 1: Comparison of gas-phase thermodynamic-property evaluation in OpenFOAM and Cantera.

	Thermodynamic properties of each species	Mixture treatment
OpenFOAM	JANAF polynomials	Requires a common midpoint temperature for all species
Cantera	JANAF polynomials	Allows species-dependent midpoint temperatures

Table 2: Comparison of gas-phase transport-coefficient evaluation in OpenFOAM and Cantera.

	Mass diffusivity	Thermal diffusivity	Dynamic viscosity
OpenFOAM	Unity-Lewis-number assumption	Eucken approximation	Sutherland law
Cantera	Kinetic theory and mixture-averaged transport		

3.2. Validation of the chemical-reaction model

One- and two-dimensional detonation-tube simulations were conducted for n-decane (n-$C_{10}H_{22}$) mixtures. Detonation velocity, CJ pressure ratio, and cell size were validated against the experimental data of [26] over a range of equivalence ratios and nitrogen dilution ratios. The mechanism used in this work is a 16-species, 18-reaction reduced mechanism derived from the 31-species, 73-reaction skeletal mechanism of [27], as listed in Appendix A. As a kerosene surrogate, n-decane is more representative of practical RDE applications than the n-heptane fuel used in previous OpenFOAM-based spray detonation work [9].

The one- and two-dimensional detonation tubes are filled with either gaseous or spray n-decane–oxygen–nitrogen mixtures in a square tube with a side length of 56.7 mm, which has the same cross-sectional area as the 64 mm diameter round tube used in [26]. For the 298 K cases, n-decane is introduced as 5 μm droplets arranged uniformly in the initial field, whereas for the 458 K cases, n-decane is treated as a gas-phase fuel. The nitrogen dilution ratio β is defined as the volume ratio of N_2 to O_2, and the equivalence ratio is denoted by ϕ. For all cases, the initial reactant pressure is 1.01325 bar. Detonation is initiated by a hot spot with a pressure of 50 bar and a temperature of 2000 K; the hot spot is placed at the left end of the one-dimensional domain and imposed as four semicircular hot spots in the two-dimensional domain. Slip-wall boundary conditions are used at the left and right ends, and cyclic boundaries are imposed in the transverse direction for the two-dimensional cases. The one-dimensional grid size is 0.1 mm. In the two-dimensional simulations, AMR is used with indicators for shocks, detonation fronts, contact surfaces, and reaction zones. The base grid size is 0.2 mm; the maximum refinement levels are four for gas-phase cases and three for spray cases. Because the droplet diameter is small, breakup model is not considered.

A series of one-dimensional cases was first computed at $\beta = 0$ with varying ϕ. The resulting CJ parameters and their comparison with experimental and theoretical values are shown in Figure 5. The theoretical CJ predictions obtained with the present reduced mechanism agree well with those obtained using the detailed mechanism adopted in [26]. The simulated detonation velocities in both gas-phase and spray mixtures agree with the CJ velocities and the experimental measurements. The spray mixtures yield slightly higher detonation velocities because their initial reactant loading density is marginally higher than that of the corresponding homogeneous gas mixture, which increases the total heat release.

The simulated CJ pressure ratios in the gas-phase and spray mixtures are similar, and both agree well with the theoretical CJ predictions and remain close to the experimental measurements. These results demonstrate that BYCSprayFoam with the 16-species, 18-reaction reduced mechanism can accurately predict the CJ characteristics of n-decane detonations.

Figure 6 compares the gas-phase and spray detonation structures for ϕ = 1.0. The spray detonation exhibits a sharper von Neumann pressure spike, higher peak pressure, and higher velocity, whereas the temperature profiles are similar. Figure 6(d) further indicates that prevaporization of n-decane ahead of the spray detonation front is negligible; the detonation is therefore sustained primarily by liquid-phase n-decane fuel.

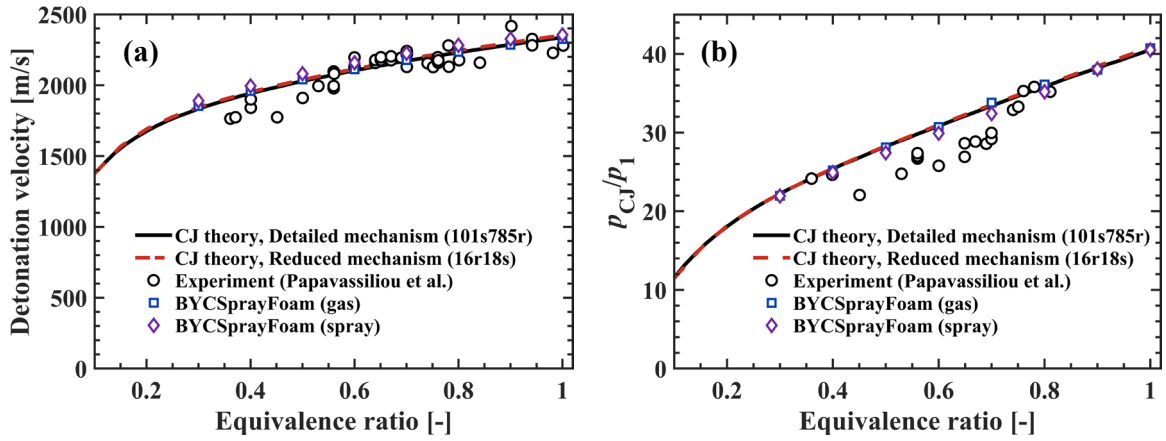

Figure 5: CJ characteristics in the one-dimensional detonation-tube cases: (a) detonation velocity; (b) CJ-point pressure ratio. Experimental data are from [26].

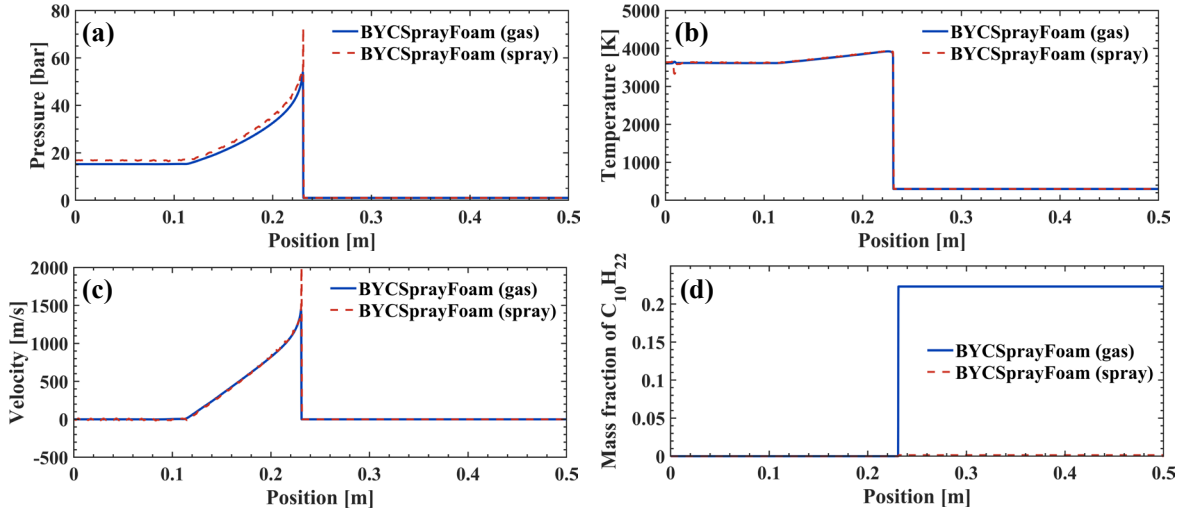

Figure 6: Flow-field comparison for the one-dimensional detonation-tube cases: (a) pressure; (b) temperature; (c) velocity; (d) gas-phase n-decane mass fraction.

A series of two-dimensional cases was then computed at ϕ = 0.9 with varying β. Figure 7 compares the predicted cell sizes with theoretical estimates and experimental measurements. The empirical formula uses $\lambda = A\ l_{ind}$ with A = 60, where λ is the predicted detonation cell size and l_{ind} is the induction-zone length. As shown in Figure 7(a), the gas-phase cell sizes predicted by BYCSprayFoam agree reasonably well with both the experimental measurements and the empirical formula. For spray mixtures, Figure

7(b) shows that the computed cell sizes are consistent with the experimental measurements and are approximately twice the gas-phase values predicted by the same empirical formula, in agreement with [26]. This behavior indicates that the induction-zone dynamics of spray detonation are strongly affected by droplet evaporation and gas–liquid interphase coupling. The results confirm that BYCSprayFoam, together with the 16-species, 18-reaction reduced mechanism, can capture the induction-zone dynamics relevant to detonation-cell formation.

Figure 8 shows maximum-pressure history maps for representative gas-phase and spray detonation cases. Although all simulations are initiated with four hot spots, the number of transverse waves adjusts naturally during propagation, generally increasing first and then decreasing toward a statistically steady pattern. At the same β, the gas-phase reactants produce significantly smaller cells than the spray reactants, and the gas-phase cellular pattern is less regular. In the spray cases, the detonation initially quenches and then reinitiates. This occurs because the stable spray detonation has a higher peak pressure, approximately 10^2 bar, and the initial hot-spot pressure of 50 bar is insufficient to maintain the wave; the curvature of the semicircular hot spots also stretches the front and promotes quenching. After the wave propagates over a finite distance, heat release accumulates in the elongated reaction zone and triggers reinitiation. The reinitiated detonation subsequently becomes self-sustained and rapidly develops transverse-wave structures. The reinitiation distance increases with beta because the reduced mixture reactivity both raises the energy required for reinitiation and lowers the heat-release rate.

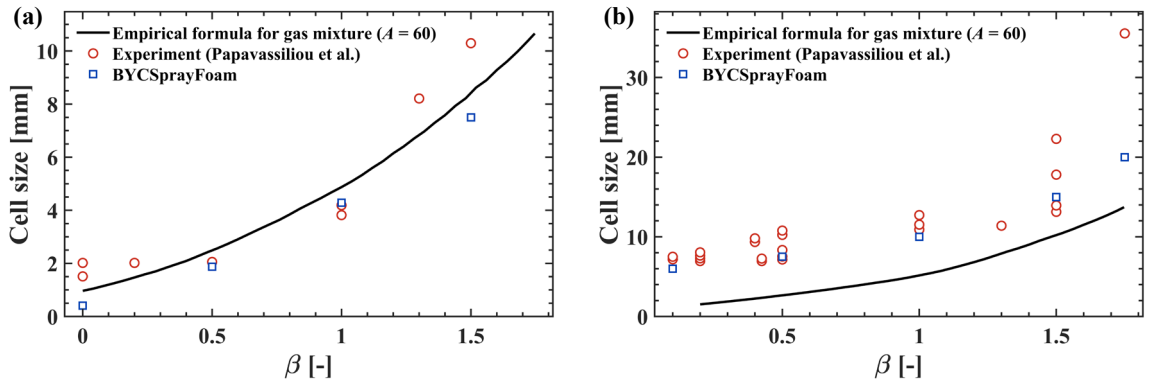

Figure 7: Detonation cell sizes in the two-dimensional detonation-tube cases: (a) gas-phase detonation; (b) spray detonation. Experimental data and the empirical formula for gas-phase mixtures are from [26].

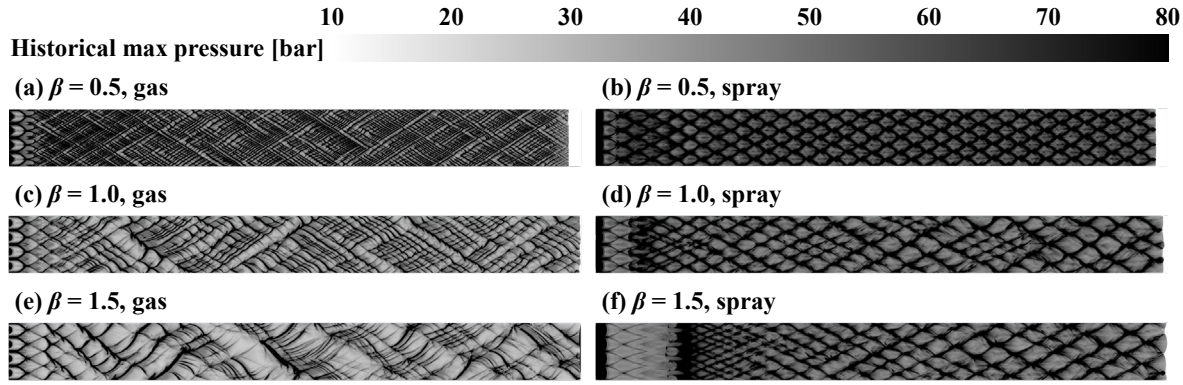

Figure 8: Maximum-pressure histories in the two-dimensional detonation-tube cases: gas-phase detonation under (a) β = 0.5, (c) β = 1.0, (e) β = 1.5; spray detonation under (b) β = 0.5, (d) β = 1.0, (f) β = 1.5.

3.3. Computational performance assessment

To assess the performance of BYCSprayFoam, a two-dimensional wedge-induced standing detonation was simulated. The domain geometry follows [28], with all lengths scaled by a factor of two. The left boundary is an inlet, where a 4000 m/s, 500 K air stream carrying 300 K n-decane droplets enters the domain. In addition to the AMR indicators used in Section 3.2, cells containing droplets are refined by requiring the liquid-phase volume fraction (sprayCloudTheta) to exceed 1×10^{-16}. The initial flow field is filled with the incoming air stream, and the calculation is advanced to 100 μs to obtain a steady flow field. Four cases listed in Table *3* were run on 64 MPI ranks. Apart from the acceleration strategies listed in the table, all numerical settings are identical. Figure 9 presents the steady flow fields and CPU times. The flow fields obtained in all cases are essentially identical, while AMR, mesh load balancing, and chemistry load balancing each reduce the computational cost. When all three strategies are enabled, the computational performance improves by approximately a factor of four, similar to the acceleration previously obtained with BYCFoam [7] under comparable refinement settings. This demonstrates that the present acceleration strategies remain effective even when the ratio of Lagrangian parcels to Eulerian cells is approximately 1.6%.

Table 3: Cases and computational settings for the performance assessment.

Case	Base mesh size [mm]	Finest mesh size [mm]	Chemistry load balancing	Mesh load balancing	Final cell count	Final parcel count
Case 1	0.4	0.1	On	On	446,523	7,276
Case 2	0.4	0.1	On	Off	443,526	7,207
Case 3	0.4	0.1	Off	Off	442,761	7,237
Case 4	0.1	0.1	Off	Off	1,620,000	7,237

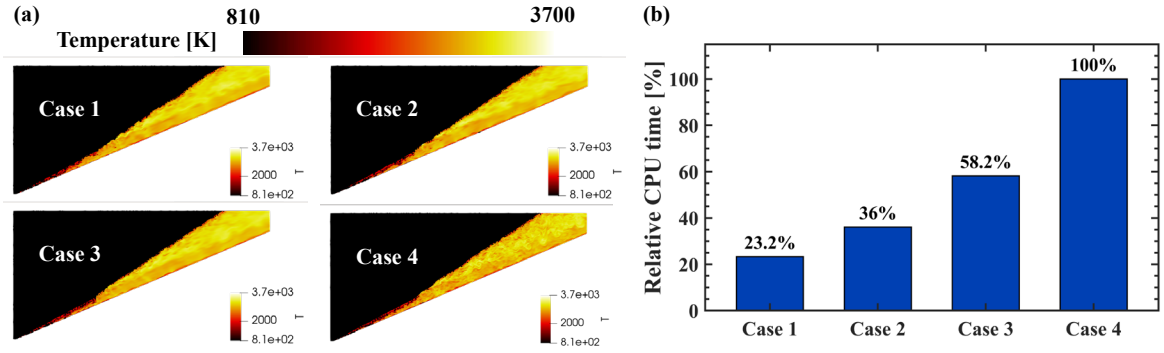

Figure 9: Performance assessment: (a) steady flow fields for different cases; (b) relative CPU time.

3.4. Three-dimensional RDE simulation

A three-dimensional non-premixed spray RDE case is simulated. The fuel is the kerosene surrogate $C_{10}H_{20}$, and the two-step global mechanism proposed by Franzelli et al. [29] is used. The annular combustor has inner and outer diameters of 368 and 400 mm, respectively; the combustor and upstream inlet duct lengths are 200 and 124 mm, respectively. The inlet duct is Laval-shaped, with a throat width of 8 mm. AMR with three refinement levels is used, giving a minimum cell size of approximately 0.5 mm, and the refinement criteria are the same as those in Section 3.3. The air inlet total pressure and total temperature are 4.5 bar and 600 K, respectively. A waveTransmissive non-reflecting outflow boundary condition is imposed at the outlet; such boundary treatments have been widely used in previous RDE

simulations. $C_{10}H_{20}$ droplets with a diameter of 100 μm are injected through a 4 × 120 array of nozzles placed at the inlet throat using coneNozzleInjection, with a total liquid-fuel mass flow rate of 391 g/s. Droplet breakup is modeled using the Reitz-KHRT model, with B1 = 1.71 following the recommendation of [30] and all other parameters kept at their standard values. Detonation is initiated by mapping a one-dimensional detonation wave in the azimuthal direction and placing a premixed region ahead of the wave. The simulation is advanced until a quasi-steady state is reached, as shown in Figure 10. At this state, the air mass flow rate is approximately 4.35 kg/s, the global equivalence ratio is approximately 1.32, and the Eulerian mesh and Lagrangian parcel counts are approximately 2.3×10^6 and 5.0×10^5, respectively.

Figure 10 shows that a continuously rotating detonation wave (RDW) is established in the combustor. Two oblique shocks extend from the RDW toward the upstream and downstream directions, and all three structures rotate synchronously. Ahead of the RDW, the $C_{10}H_{20}$ droplets mix with the incoming air and form a detonable mixture. The interface between the burned gas and the fresh mixture behaves as a deflagration front. Heat transfer from this front vaporizes part of the $C_{10}H_{20}$ droplets upstream of the interface; the resulting vapor subsequently burns, causing the contact surface to become more wrinkled than that typically observed in purely gas-phase RDE simulations.

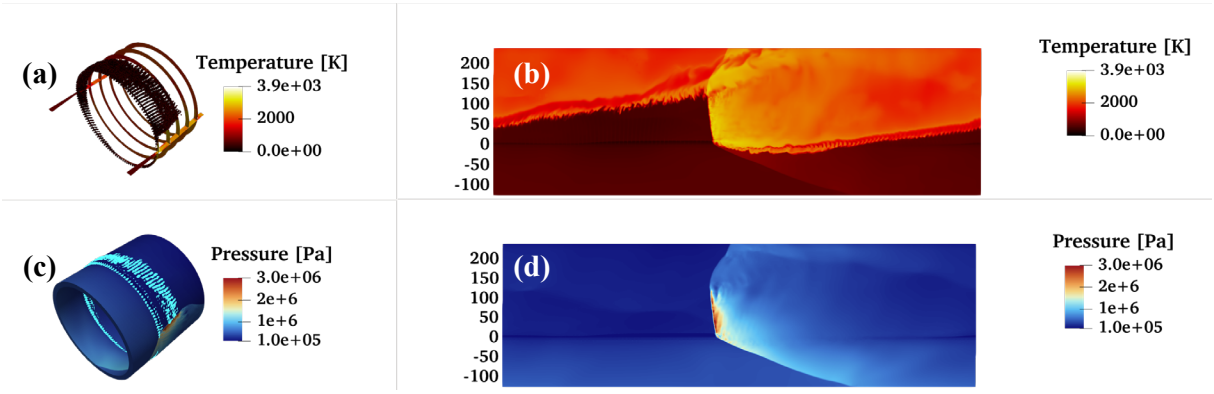

Figure 10: Non-premixed RDE simulation. (a) Temperature distribution on the meridional plane, cross sections at z = 1, 50, 100, 150, and 200 mm, and Lagrangian parcel temperature; (b) unfolded temperature field on the r = 192 mm surface; (c) surface pressure distribution, with Lagrangian parcels marked in light blue; (d) unfolded pressure field on the r = 192 mm surface.

4. Conclusions

Standard model problems were first simulated and compared with experimental data to verify the two-way coupling between the Cantera thermophysical module and the OpenFOAM droplet submodels. The results show that BYCSprayFoam improves the accuracy of heat- and mass-transfer predictions relative to solvers relying on OpenFOAM native thermophysical models, while retaining comparable accuracy for momentum exchange. One- and two-dimensional detonation-tube simulations were then used to validate the CJ parameters and cell sizes against experimental and theoretical references, confirming the capability of the reduced n-decane mechanism and BYCSprayFoam to reproduce key detonation characteristics. A two-dimensional wedge-induced standing-detonation case demonstrated the acceleration achieved by AMR, mesh load balancing, and chemistry load balancing; the maximum speedup in the present tests is approximately four, comparable to that obtained previously for purely Eulerian gas-phase simulations. Finally, a three-dimensional non-premixed spray RDE was simulated, and a self-sustained rotating detonation wave was obtained. Overall, BYCSprayFoam provides an accurate and efficient Euler–Lagrange framework for gas–liquid two-phase rotating-detonation simulations.

Acknowledgements

This study was funded by the National Natural Science Foundation of China (Grant Nos. 52506121 and 52076003). The authors also acknowledge Miao Cheng for his assistance.

References

[1] J. Sun, Y. Wang, B. Tian, and Z. Chen, "detonationFoam: An open-source solver for simulation of gaseous detonation based on OpenFOAM," *Computer Physics Communications,* vol. 292, p. 108859, 2023/11/01/ 2023, doi: https://doi.org/10.1016/j.cpc.2023.108859.

[2] V. B, "Stationary Spin Detonation," *Soviet Journal of Applied Mechanics and Technical Physics,* vol. 3, no. 3, pp. 157-164, 1960.

[3] M. Luan, S. Zhang, Z. Xia, S. Yao, and J. P. Wang, "Analytical and numerical study of the expansion effect on the velocity deficit of rotating detonation waves," *Combustion Theory and Modelling,* vol. 24, no. 4, pp. 761-774, 2020/07/03 2020, doi: 10.1080/13647830.2020.1758346.

[4] J. Z. Ma *et al.*, "Recent Progress, Development Trends, and Consideration of Continuous Detonation Engines," *AIAA Journal,* vol. 58, no. 12, pp. 4976-5035, 2020, doi: 10.2514/1.J058157.

[5] J. Kindracki, "Experimental research on rotating detonation in liquid fuel–gaseous air mixtures," *Aerospace Science and Technology,* vol. 43, pp. 445-453, 2015/06/01/ 2015, doi: https://doi.org/10.1016/j.ast.2015.04.006.

[6] P. Wolański, W. Balicki, W. Perkowski, and A. Bilar, "Experimental research of liquid-fueled continuously rotating detonation chamber," *Shock Waves,* vol. 31, no. 7, pp. 807-812, 2021/10/01 2021, doi: 10.1007/s00193-021-01014-w.

[7] M. Cheng, Z. Sheng, and J.-P. Wang, "BYCFoam: An Improved Solver for Rotating Detonation Engines Based on OpenFOAM," *Energies,* vol. 17, no. 4, p. 769, 2024. [Online]. Available: https://www.mdpi.com/1996-1073/17/4/769.

[8] S. Subramaniam, "Lagrangian–Eulerian methods for multiphase flows," *Progress in Energy and Combustion Science,* vol. 39, no. 2, pp. 215-245, 2013/04/01/ 2013, doi: https://doi.org/10.1016/j.pecs.2012.10.003.

[9] Z. Huang, M. Zhao, Y. Xu, G. Li, and H. Zhang, "Eulerian-Lagrangian modelling of detonative combustion in two-phase gas-droplet mixtures with OpenFOAM: Validations and verifications," *Fuel,* vol. 286, p. 119402, 2021/02/15/ 2021, doi: https://doi.org/10.1016/j.fuel.2020.119402.

[10] H. Chen, M. Zhao, H. Qiu, and Y. Zhu, "Implementation and verification of an OpenFOAM solver for gas-droplet two-phase detonation combustion," *Physics of Fluids,* vol. 36, no. 8, 2024, doi: 10.1063/5.0221308.

[11] G. Strang, "On the Construction and Comparison of Difference Schemes," *SIAM Journal on Numerical Analysis,* vol. 5, no. 3, pp. 506-517, 1968, doi: 10.1137/0705041.

[12] D. G. Goodwin, H. Moffat, and R. L. Speth, "Cantera: An Object-oriented Software Toolkit for Chemical Kinetics, Thermodynamics, and Transport Processes. Version 2.2.1," 2016.

[13] R. J. C. Kee, M.E.; Glarborg, P.; Zhu, H., "Front Matter," in *Chemically Reacting Flow: Theory, Modeling, and Simulation*, J. W. Sons. Ed. New York, NY, USA, 2017, pp. i-xli.

[14] R. C. Reid, T. K. Sherwood, and R. E. Street, "The Properties of Gases and Liquids," 1977.

[15] A. Kurganov, S. Noelle, and G. Petrova, "Semidiscrete Central-Upwind Schemes for Hyperbolic Conservation Laws and Hamilton-Jacobi Equations," *SIAM J. Sci. Comput.,* vol. 23, pp. 707-740, 2001.

[16] A. Harten, P. D. Lax, and B. v. Leer, "On Upstream Differencing and Godunov-Type Schemes for Hyperbolic Conservation Laws," *SIAM Review,* vol. 25, no. 1, pp. 35-61, 1983, doi: 10.1137/1025002.

[17] E. F. Toro, M. Spruce, and W. Speares, "Restoration of the contact surface in the HLL-Riemann solver," *Shock Waves,* vol. 4, no. 1, pp. 25-34, 1994.

[18] F.-j. C. Shu-sheng Chen, Hai-chao Xue, Ning Wang, Chao Yan, "An improved AUSM-family scheme with robustness and accuracy for all Mach number flows," *Applied Mathematical*

Modelling, vol. Volume 77, Part 2, pp. Pages 1065-1081, 2020, doi: https://doi.org/10.1016/j.apm.2019.09.005.

[19] A. JAMESON, "Time dependent calculations using multigrid, with applications to unsteady flows past airfoils and wings," in *10th Computational Fluid Dynamics Conference*.

[20] D. Rettenmaier *et al.*, "Load balanced 2D and 3D adaptive mesh refinement in OpenFOAM," *SoftwareX,* vol. 10, p. 100317, 2019, doi: 10.1016/j.softx.2019.100317.

[21] *swak4Foam: SWiss Army Knife for Foam*. (2026). SourceForge. Accessed: 2026/06/12. [Online]. Available: https://sourceforge.net/p/openfoam-extend/swak4Foam/ci/default/tree/

[22] W. E. Ranz and W. R. Marshall, Jr., "Evaporation from drops. Part I," *Chemical Engineering Progress,* vol. 48, pp. 141-146, 1952. [Online]. Available: https://ia801301.us.archive.org/32/items/ranz-marshall.-evaporation-from-drops-i-and-ii/Ranz-Marshall.%20Evaporation%20from%20Drops%20I%20and%20II.pdf.

[23] H. Watanabe, A. Matsuo, K. Matsuoka, A. Kawasaki, and J. Kasahara, "Numerical investigation on propagation behavior of gaseous detonation in water spray," *Proceedings of the Combustion Institute,* vol. 37, no. 3, pp. 3617-3626, 2019/01/01/ 2019, doi: https://doi.org/10.1016/j.proci.2018.07.092.

[24] P. A. Strizhak, R. S. Volkov, G. Castanet, F. Lemoine, O. Rybdylova, and S. S. Sazhin, "Heating and evaporation of suspended water droplets: Experimental studies and modelling," *International Journal of Heat and Mass Transfer,* vol. 127, pp. 92-106, 2018/12/01/ 2018, doi: https://doi.org/10.1016/j.ijheatmasstransfer.2018.06.103.

[25] J. D. Sartor and C. E. Abbott, "Prediction and Measurement of the Accelerated Motion of Water Drops in Air," (in English), *Journal of Applied Meteorology and Climatology,* vol. 14, no. 2, pp. 232-239, 01 Mar. 1975 1975. [Online]. Available: https://journals.ametsoc.org/view/journals/apme/14/2/1520-0450_1975_014_0232_pamota_2_0_co_2.xml.

[26] J. Papavassiliou, A. Makris, R. Knystautas, J. H. S. Lee, C. K. Westbrook, and W. J. Pitz, "Measurements of Cellular Structure in Spray Detonation," in *Dynamic Aspects of Explosion Phenomena*, vol. 154. Washington, DC: American Institute of Aeronautics and Astronautics, 1993, pp. 148-169.

[27] S. Xiong and Y. Bi, "A Novel Multi-Step Global Mechanism Scheme for n-Decane Combustion," *Entropy,* vol. 25, no. 10, p. 1389, 2023. [Online]. Available: https://www.mdpi.com/1099-4300/25/10/1389.

[28] Y.-J. Wu and Y.-Y. Niu, "Impact of Intermediate Species in Simulating Oblique Detonation with Pre-Vaporized N-Decane/air Mixtures Substituting for Kerosene/Air Mixtures," *Combustion Science and Technology,* vol. 197, no. 16, pp. 4140-4165, 2025/12/10 2025, doi: 10.1080/00102202.2024.2362312.

[29] B. Franzelli, E. Riber, M. Sanjosé, and T. Poinsot, "A two-step chemical scheme for kerosene–air premixed flames," *Combustion and Flame,* vol. 157, no. 7, pp. 1364-1373, 2010/07/01/ 2010, doi: https://doi.org/10.1016/j.combustflame.2010.03.014.

[30] W. Wang, M. Yang, Z. Hu, and P. Zhang, "A dynamic droplet breakup model for Eulerian-Lagrangian simulation of liquid-fueled detonation," *Aerospace Science and Technology,* vol. 151, p. 109271, 2024/08/01/ 2024, doi: https://doi.org/10.1016/j.ast.2024.109271.

Appendix A: Chemical Reaction Model

Table A.1 Reduced chemical reaction mechanism for $C_{10}H_{22}$. Units are [s, mol, cm^3, K]; E is in kcal/mol. The forward rate coefficient is $k_f = AT^{\beta} \exp(-E/RT)$.

No.	Reaction	A	β	E
1	$H + O_2 \rightleftharpoons OH + O$	9.756×10^{10}	0.00	14.842
2	$H + O_2 + M \rightleftharpoons HO_2 + M$	3.535×10^{12}	-0.80	0
3	$HO_2 + H \rightleftharpoons 2\ OH$	1.686×10^{11}	0.00	0.875
4	$CO + OH \rightleftharpoons CO_2 + H$	8.97×10^{3}	1.50	-0.741
5	$CO + HO_2 \rightleftharpoons CO_2 + OH$	1.51×10^{11}	0.00	23.638
6	$HCO + M \rightleftharpoons CO + H + M$	7×10^{11}	0.00	16.802
7	$HCO + OH \rightleftharpoons CO + H_2O$	1.024×10^{12}	0.00	0
8	$HCO + O_2 \rightleftharpoons CO + HO_2$	3.011×10^{9}	0.00	0
9	$CH_2O + OH \rightarrow HCO + H_2O$	3.433×10^{6}	1.18	-0.454
10	$CH_3 + O \rightleftharpoons CH_2O + H$	8.43×10^{10}	0.00	0
11	$CH_3 + O_2 \rightleftharpoons CH_2O + OH$	3.3×10^{8}	0.00	8.939
12	$C_2H_4 + O \rightleftharpoons CH_3 + HCO$	1.355×10^{4}	1.88	0.179
13	$C_2H_5 + O_2 \rightleftharpoons C_2H_4 + HO_2$	1.024×10^{7}	0.00	-2.187
14	$C_3H_6 + OH \rightleftharpoons C_2H_5 + CH_2O$	7.9×10^{9}	0.00	0
15	$C_{10}H_{22} \rightarrow C_3H_6 + 3\ C_2H_4 + CH_3 + H$	5.732×10^{16}	0.00	81.919
16	$C_{10}H_{22} + O_2 \rightarrow C_3H_6 + 3\ C_2H_4 + CH_3 + HO_2$	6×10^{11}	0.00	47.562
17	$C_{10}H_{22} + OH \rightarrow C_3H_6 + 3\ C_2H_4 + CH_3 + H_2O$	2.6×10^{4}	2.00	-0.765
18	$C_{10}H_{22} + O \rightarrow C_3H_6 + 3\ C_2H_4 + CH_3 + OH$	6.5×10^{10}	0.00	5.21

Notes:

1. The symbol "⇌" denotes a reversible reaction, and "→" denotes an irreversible reaction.

2. For all three-body reactions in the table (Reactions 2 and 6), the collision efficiencies are N_2: 0.40, O_2: 0.40, H_2O: 6.50, CO: 0.75, CO_2: 1.50, $C_{10}H_{22}$: 3.00.